

Comprehensive assessment of particle-scale modelling for biomass pyrolysis: One-dimensional versus three-dimensional models

Teresa Martí-Rosselló,[†] Jun Li,^{*,†} Leo Lue,[†] Oskar Karlström,[‡] and Anders Brink[¶]

[†]*Department of Chemical and Process Engineering, University of Strathclyde, James Weir Building, 75 Montrose Street, Glasgow G1 1XJ, United Kingdom*

[‡]*Johan Gadolin Process Chemistry Center, Åbo Akademi University, Piispankatu 8, FI-20500, Turku, Finland*

[¶]*Process and Systems Engineering, Åbo Akademi University, Piispankatu 8, FI-20500, Turku, Finland*

E-mail: jun.li@strath.ac.uk

Abstract

The present work examines the impact of the dimensionality of single particle models (SPMs) for the pyrolysis of thermally-thick biomass particles. It builds up comprehensive one-dimensional and three-dimensional SPMs and assesses their performances to gain a systematic understanding of the accuracy of predicted results, predictive capability, and computational costs. Cylindrical wheat straw pellets with an average size of 1 cm length and 7 mm diameter were studied on their pyrolysis performances at temperatures ranged from 200 to 700°C. It investigates the correlation between the inner heating rate of the particle and the resulting irregular porosity distribution in the

pyrolyzed particle. The predictions of the model are in good agreement with the experimental measurement, and they show that the predicted char yield is not sensitive to the model dimensionality but the rate of mass loss and the char porosity are. Additionally, the three-dimensional single particle model is found to be compatible with a wider range of biomass types. The model captures a higher heating rate at the surface and at the center of the particle as compared to the region in between. This is linked to an uneven porosity distribution in the pyrolyzed particle, which is higher at the surface and at the center of the particle. While the three-dimensional SPM provides a small improvement in the prediction of the temperature profile, as compared to the one-dimensional model, and offers additional details (e.g., temperature distribution, heating rate, and porosity distribution inside the particle), it required significantly greater computational times, which might not be justifiable in many situations.

1 Introduction

Biomass pyrolysis is a thermochemical conversion technology from which a range of products of interest can be obtained. Pyrolysis consists of heating the biomass feedstock in the absence of oxygen in order to obtain solid (char), gas and liquid products (tar, bio-oil), which distribution highly depends on the operating conditions, as well as the fuel characteristics. Prior to the pyrolysis process, biomass is typically ground or shredded, but the particles are often thermally thick in diverse sizes and shapes. Thermally thick particles are usually characterized by the Biot number, with an apparent temperature gradient inside the particle during the heating process. The shape and the size of the biomass particles determine the intra-particle heat and mass transfer processes, which in turn influence the distribution and characteristics of the product yields. At the particle level, the potential impact of the shape and size of a biomass particle on the pyrolysis performance, is mathematically studied with a single particle model (SPM). SPM requires a input of various parameters, for example, enthalpies of formation of char and tar, the heat transfer coefficient, and the thermal

conductivity of the biomass,¹ some of them are difficult to determine from the experiments and thus usually assumed from the literature. According to Blasi,² the biomass properties have a major impact on the modelling of biomass conversion when the biomass particles are large and they fall into the category of thermally thick regime, whilst the influence of the biomass and char permeabilities is not as significant as the influence of the biomass density and the biomass thermal conductivity.

Single particle models (SPMs) are used to determine the significance of the model assumptions, the impact of the biomass properties and the operating conditions on the pyrolysis process, and to understand how the kinetics and the transfer phenomena interact.^{2,3} SPMs study the heat and mass transfer inside a large biomass particle, and how they affect the final product yields of pyrolysis. The predictive capability of a single particle model has been found to be highly dependent on the assumptions of process kinetics and biomass properties.² Some of the common assumptions in the SPMs found in the literature are that (1) the particle is a solid with a void fraction (porosity), (2) both the solid and the vapor phase are in thermal equilibrium, (3) the particle does not shrink or break, (4) the heat is transferred from the reactor environment to the particle by thermal radiation and thermal convection, the heat travels through the particle by conduction, and that (5) the volatiles generated behave like an ideal gas and (6) are released from the particle driven by a pressure gradient (mass convection), but their diffusion can be neglected.

Most SPMs were based on woody biomass particles, assuming a spherical particle shape, where the heat and mass transfer processes happen symmetrically, with products lumped in groups according to their phase (vapor phase or solid phase) and the vapor phase separated into bio-oil and gas. Research attempts have been also made to implement additional or complex features on their particle models. Corbetta et al.⁴ implemented a detailed kinetic mechanism into a SPM, including secondary pyrolysis reactions. The kinetic mechanism was based on the one previously published by Ranzi et al.⁵ in which the biomass components and the pyrolysis products were given in the empirical formula of their representative

molecule. Shrinkage was included in the model from Anca-Cuoce et al.⁶ and in the model from Babu et al.,⁷ using a correlation for shrinking that depends on the degree of mass loss. Park et al.⁸ experimentally studied the breakage of woody particles undergoing pyrolysis, and to that end they used a SPM to report information related to the distribution and evolution of the particle inner pressure and the char yield. Some studies have not made the assumption of thermal equilibrium between the gas phase and the solid phase,^{9,10} but the reasons or potential gain in accuracy have not been discussed.

The majority of SPMs available in the literature for biomass thermochemical conversions are one dimensional. However, SPMs in one dimension can not effectively describe the diverse shape of biomass particles other than the spherical ones, although numerical tricks, e.g., the use of shape factors, could be applied to reflect the actual mass or heat transfer of cylinder or slab particles. To gain an adequate description of the anisotropic structure of lignocellulosic materials and to quantify its implications in the pyrolytic degradation, Di Blasi¹¹ developed a two-dimensional SPM to study the pyrolysis of wood particles and compared against a one-dimensional SPM. The model dimensionality comparison showed that the conversion time is shorter and the volatiles yield is larger in the case of the two-dimensional model.² Ciesielski et al.¹² used a three-dimensional SPM to capture the particle microstructure with its irregular pore sizes and directions of the porosity channels. Solving all the corresponding heat and mass transfer processes of biomass pyrolysis with such a complex geometry carries an increase in computational workload, therefore they only included the heat transfer process of heat conduction, and the mass transfer process of mass diffusion, excluding chemical reactions. More recently, Wickramaarachchi et al.¹³ developed a three-dimensional model to examine the spatial variations during the pyrolysis process, however the modelling approach was rather simplified assuming the pressure inside the particle is atmospheric pressure, which is unable to predict the transport of released volatiles. Gentile et al.¹⁴ developed a three-dimensional numerical framework, called bioSMOKE, for the modelling pyrolysis of anisotropic woody biomass particles of different shapes, using a dynamic mesh

algorithm to reflect arbitrary deformations of the shape of the domain, however, the overall computational costs were not discussed and thus unable to gain an understanding of its feasibility for wider applications.

As computational power increases, interests in development of three-dimensional SPMs are growing to express the actual situations as the pyrolysis process of thermally thick biomass particles. It is crucial to gain an insightful understanding of the real impact of particle shape, anisotropy and porosity on the transport phenomena, however, this might require a significant increase of computational costs and may take unrealistically long to acquire modelling results from complex SPMs. A comprehensive assessment of the impact of dimensionality of the SPMs is therefore needed to assist the selection of a right particle-scale modelling to meet various demands in different applications.

Aiming to address the identified gaps, this work builds up comprehensive one-dimensional and three-dimensional SPMs for studies of pyrolysis of thermally-thick biomass particles, and assesses their performances to gain a systematic understanding of the accuracy of predicted results, predictive capability, and computational costs, etc. The SPMs are solved using the finite element method, and validated by single particle experiments of wheat straw under well controlled pyrolysis conditions. The model dimensionality is compared not only in terms of inner heating, but also in terms of mass loss and char yield. The modelling results have shown not only depict the inner temperature profile, but also the inner heating rate of the particle, and the inner heating rate behaviour is linked to the porosity distribution.

2 Experimental procedure

The biomass samples used in this work are wheat straw pellets purchased from Agripellets Ltd. Table 1 gives the pellet characterization and Fig. 1 shows a picture of a pellet with the pellet dimensions. The pellets were measured and sometimes their length was modified in order to use an average pellet size of 1 cm length and 7 mm diameter. The pellets were dried

Table 1: Physical and chemical characterization of wheat straw as given by Agripellets Ltd. Moisture (M), ash, and higher heating value (HHV) are presented in 'as received' basis (*ar*) and the rest in dry ash-free basis (*daf*).

Proximate analysis wt%				Ultimate analysis ^{daf} wt%						HHV ^{ar}
M ^{ar}	Ash ^{ar}	VM ^{daf}	FC ^{daf}	C	H	O	N	S	Cl	MJ kg ⁻¹
9.3	6.7	80.8	19.2	48.8	5.67	44.5	0.77	0.16	0.13	17.2

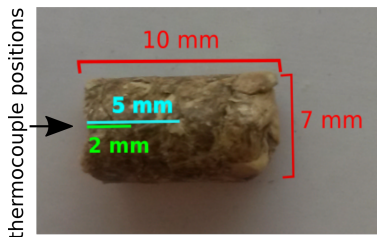


Figure 1: Wheat straw pellet dimensions (red lines) and inner thermocouple positions (blue and green lines).

overnight at 105°C and kept in a desiccator cabinet. The bulk density of the dry pellet is approximately 780 kg m⁻³, and it was determined using the average pellet mass of 0.3 g and the average pellet volume of 3.8×10^{-7} m³.

A scheme of the single particle reactor used in this work can be found in Fig. 2, it consists of a quartz tube reactor inserted in a ceramic furnace that is electrically heated. The inner diameter of the reactor is 0.0443 m. A more detailed description of the device can be found elsewhere.^{15,16} The volumetric flow of the carrier gas is 220 L h⁻¹ for all the experiments, and the gas used is nitrogen. The pellet is placed in a platinum basket holder, which has been assumed to not interfere with the heat transfer. The pellet was first introduced in a lateral quartz arm and kept there until all the oxygen was vented out before moving the pellet at the center of the reactor in the reacting zone. After pyrolysis, the pellet was pulled out of the center and kept at the lateral arm until it cooled with nitrogen gas to avoid further decomposition. The experimental measurements taken were the pellet mass loss and the pellet inner temperature.

To measure the pellet mass loss due to pyrolysis with time, multiple pellets were individ-

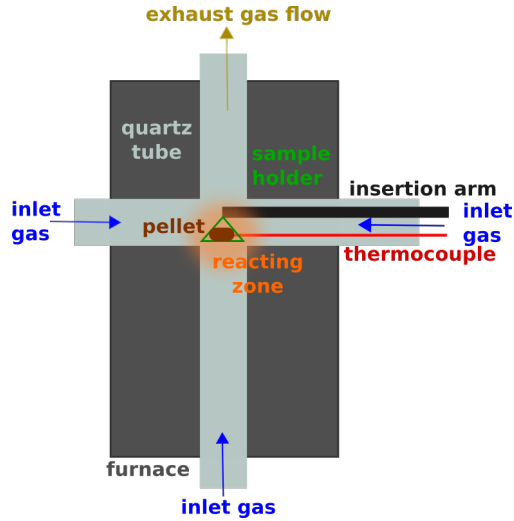


Figure 2: Diagram of the single particle reactor.

ually pyrolyzed and extracted from the reactor at different times and consecutively weighted with a scale. The scale has a maximum error of ± 0.05 mg, taking into account that the weight of the holder with the sample is about 0.7–0.8 g, it entails a very small percentage error below 1%. The temperature inside the pellet was obtained by inserting a thermocouple at a designated position in the pellet and recording the measured temperature. To obtain the temperature information from a different inner position in the pellet, a repetition of the experiment was carried on. The selected positions were at 2 and 5 mm (center) from an end of the pellet (see Fig. 1). The temperature at 2 mm gives additional information about the pellet inner temperature distribution.

3 Numerical model

3.1 System description

The system is defined as a porous particle. The particle consists of a solid phase and a void fraction ε . The effect of the reactor on the particle is captured by the imposed boundary conditions at the surface. The main reactor conditions captured are the temperature of the reactor environment T_∞ , and the media in the reactor environment, which is nitrogen

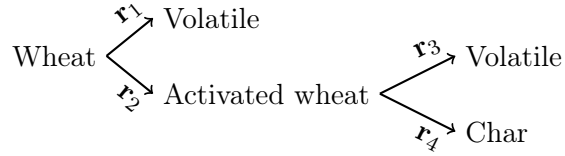


Figure 3: Diagram of the kinetic mechanism.

flowing and taking away all the volatile products released from the particle. The voids are filled with the vapor phase, which includes the initial nitrogen and the volatiles generated. The generation of volatiles is controlled by the temperature of the particle, but their release from the particle once they have been generated, is driven by the pressure gradient inside the particle. The vapor phase is assumed to obey the ideal gas law, and its motion obeys Darcy's law, which depends on the particle's permeability κ and on the pressure gradient in the particle.

The pressure inside the particle increases because the nitrogen filling the porosity heats and expands, and also due to the generation of volatiles. Once the nitrogen in the porosity and the generated volatiles are released from the particle, the particle's inner pressure returns back to atmospheric pressure. A constant permeability is assigned to biomass, and a higher constant permeability is assigned to char (Table 3). The particle starts heating and reacting from the surface, generating char as it reacts and increasing the particle's permeability inwards. The difference in permeabilities directs the volatiles flow in the outwards direction until they are expelled from the particle.

In this model, we assume that the solid and the vapor phases are in thermal equilibrium, therefore there is only a single model temperature (T) that describes both, the temperature of the solid and the gas phase. The energy balance describes the surface heating of the particle according to a given reactor temperature, by heat convection and thermal radiation. The heat is then transferred from the surface of the particle to its center by conduction. The enthalpy of the pyrolysis reactions can also influence the temperature of the particle by generating or consuming energy in the form of heat.

Table 2: Kinetic parameters of wheat straw pyrolysis.¹⁷

	r_1	r_2	r_3	r_4
A / s^{-1}	1.1×10^5	1.2×10^3	1.2×10^3	2.82
$E / \text{kJ mol}^{-1}$	75.1	53.55	66.53	27.61

The kinetic mechanism used in this work (see Fig. 3 and Table 2) was proposed by Lanzetta et al.¹⁷ and starts from a single component that decomposes with parallel, multi-step and first-order reactions. It consists of four reactions (r_1, r_2, r_3, r_4) and four components, including wheat straw, activated wheat straw, char, and volatile. The volatile lumps the liquid and gas products. For the purpose of this paper, the enthalpies of each reaction used in this study are $\Delta H_{r_1} = 50 \text{ kJ kg}^{-1}$, $\Delta H_{r_2} = 0 \text{ kJ kg}^{-1}$, $\Delta H_{r_3} = -100 \text{ kJ kg}^{-1}$ and $\Delta H_{r_4} = -100 \text{ kJ kg}^{-1}$. Depending on which reactions are favored, the predicted temperature of the particle will be affected by the reactions' exothermicity or endothermicity. The selected enthalpies of reaction were based on values from the literature⁸ but adjusted to get a better particle temperature fit against the measured temperature profile of particle.

The evolution of the components that appear in the kinetic mechanism is described with the mass balance. Another component that is not included in the reaction mechanism but is present in the system is the nitrogen inside the pores, which is initially present in the particle before it is displaced by the volatile generated. The nitrogen release follows the same principles as the volatile release, therefore its evolution is rendered with the same mass balance.

To save the overall computational time, a lumped pyrolysis reaction mechanism was employed in this work. Given that the volatiles generated are constantly swept away from the reacting area, secondary reactions of the volatiles with the char or with other volatiles were not considered. The values of the parameters used in the single particle model are either given in Table 3 or determined with the following expressions. The convective heat

transfer coefficient is obtained with

$$h = \frac{\text{Nu} \lambda_{N_2}}{CL} \quad (1)$$

where CL is the particle characteristic length, which in the case of a spherical or a cylindrical particle, the particle diameter could be used instead, λ_{N_2} is the thermal conductivity of nitrogen, because nitrogen is the carrier gas used in the reactor, and Nu is the Nusselt number, which has been determined using the Churchill-Bernstein correlation¹⁸

$$\text{Nu} = 0.3 + \frac{0.62 \text{Re}^{1/2} \text{Pr}^{1/3}}{\left[1 + (0.4/\text{Pr})^{2/3}\right]^{1/4}} \left[1 + \left(\frac{\text{Re}}{282000}\right)^{5/8}\right]^{4/5} \quad (2)$$

where Pr is the Prandtl number, and Re is the Reynolds number. This correlation is used to determine the Nusselt number of a cylinder in a convective flow that causes heat transfer between the solid body and the flow. It is valid for a wide range of Pr and Re as long as Pr times Re is larger or equal to 0.2. The Prandtl number is a dimensionless number used in systems where there is heat transfer between a particle and a carrier gas, is defined as

$$\text{Pr} = \frac{C_{p,N_2} \mu_{N_2}}{\lambda_{N_2}} \quad (3)$$

where μ_{N_2} is the dynamic viscosity of nitrogen, and the heat capacity and thermal conductivity also refer to the carrier gas. The Reynolds number is

$$\text{Re} = \frac{\rho_{N_2} \mathbf{v}_{N_2} d_p}{\mu_{N_2}} \quad (4)$$

where \mathbf{v}_{N_2} is the velocity calculated from the nitrogen flow rate and the cross-sectional area of the reactor. The range of Re in this problem is between 3.6 and 6.7, and Pr is 0.795, which makes suitable the correlation of choice for the Nusselt number.

The model parameters that refer to the particle and that appear in Table 3 are the

Table 3: Thermophysical properties used in the single particle model. The values are obtained from the cited sources or measured (M).

Parameter	Value or expression	Notes
$d_{particle}$	0.007 m	M
$\rho_{s,0}$	780 kg m^{-3}	M
ε_0	0.22	M
T_0 ($T_\infty = 200$)	35°C	M
T_0 ($T_\infty = 300$)	40°C	M
T_0 ($T_\infty = 400$)	50°C	M
T_0 ($T_\infty = 500$)	60°C	M
T_0 ($T_\infty = 600$)	70°C	M
T_0 ($T_\infty = 700$)	70°C	M
$C_{p,B} / \text{J kg}^{-1} \text{K}^{-1}$	$2300 - 1150e^{-0.0055T}$	19
$C_{p,C} / \text{J kg}^{-1} \text{K}^{-1}$	$1430 + 0.355T - 7.3210^7 T^{-2}$	19
$C_{p,G} / \text{J kg}^{-1} \text{K}^{-1}$	$770 + 0.629T + 1.91 \cdot 10^{-4} T^2$	20
$C_{p,T} / \text{J kg}^{-1} \text{K}^{-1}$	$-100 + 4.4T - 1.57 \cdot 10^{-3} T^2$	20
$C_{p,V} / \text{J kg}^{-1} \text{K}^{-1}$	$0.85C_{p,T} + 0.15C_{p,G}$	8
$\lambda / \text{W m}^{-1} \text{K}^{-1}$	$\lambda_{cond} + \lambda_{rad}$	21
	$\lambda_{cond} = \varepsilon\lambda_V + \frac{\rho_B}{\rho_{B,0}}\lambda_B + (1 - \frac{\rho_B}{\rho_{B,0}})\lambda_C$	
	$\lambda_V = 0.026$	21
	$\lambda_B = 0.11$ or $\lambda_B = 0.15$	21
	$\lambda_C = 0.071$	21
	$\lambda_{rad} = \frac{\varepsilon\sigma T^3 d_{pore}}{\epsilon}$	
	$\epsilon = 0.9$	21
	$d_{pore} = 3.2 \times 10^{-6}$	21
κ / m^2	$\frac{\rho_B}{\rho_{B,0}}\kappa_B + (1 - \frac{\rho_B}{\rho_{B,0}})\kappa_C$	
	$\kappa_B = 5 \times 10^{-16}$	22
	$\kappa_C = 10^{-13}$	22
μ_{N_2} (Pa s)	3.5×10^{-5}	
MW_{N_2}	$0.028 \text{ kg mol}^{-1}$	
λ_{N_2}	$0.04 \text{ W m}^{-1} \text{K}^{-1}$	

initial bulk density of the solid part of the particle $\rho_{s,0}$, the diameter $d_{particle}$, the initial porosity ε_0 , the initial temperature T_0 , the heat capacity C_p , the thermal conductivity λ , and the permeability κ . The remaining model parameters are the nitrogen viscosity ν_{N_2} , the molecular weight of nitrogen MW_{N_2} , and the thermal conductivity of nitrogen λ_{N_2} .

The initial porosity is calculated as $\varepsilon_0 = 1 - \rho_{specific}/\rho_{bulk}$, where ρ_{bulk} is the bulk density which includes the porosity, and it can be easily measured from the pellet size and the pellet weight, and $\rho_{specific}$ is the specific density, which would be the particle's density without

including the porosity. The specific density of wheat straw that has been used is 1000 kg m^{-3} , which is an average value of the measurements obtained using a pycnometer of 1100 kg m^{-3} ²³ and 983 kg m^{-3} .²⁴

The initial particle temperature T_0 used in the model corresponds to the temperature measured by the thermocouple when the particle is in the lateral arm of the reactor, before it is introduced into the reaction area. Depending on the reactor temperature, the heat that the lateral arm receives might vary. The heat capacity of the particle is described by correlations that depend on the temperature, and each component has a different heat capacity; $C_{p,B}$ is the heat capacity of the biomass including wheat and activated wheat, $C_{p,C}$ is the heat capacity of char, and $C_{p,V}$ is the heat capacity of the volatiles, determined as a linear combination of the individual heat capacities of tar and gas. The thermal conductivity in the model is described with a correlation that depends on the individual thermal conductivities of the components, and it also includes the influence of the thermal radiation λ_{rad} assuming a constant pore size d_{pore} . The permeability is also given by a correlation that depends on how the solid fraction changes. Two thermal conductivities are compared in the SPM. The thermal conductivities compared are $0.15 \text{ W m}^{-1} \text{ K}^{-1}$,²⁵ which was experimentally determined for a wheat straw pellet, and $0.11 \text{ W m}^{-1} \text{ K}^{-1}$, which was used in the SPM from Lu et al.²⁴

The parameters used in the one-dimensional model and the three-dimensional model are the same, except for the diameter of the particle that in the case of a sphere it would be of 0.009 m , which corresponds to a spherical particle of the same volume as the cylindrical particle with a diameter of 0.007 m . The one-dimensional mesh consists of 20 intervals and 21 vertices, and the calculating time step was set as 10^{-5} s . While the three-dimensional mesh used to describe a cylinder consists of 25663 tetrahedral elements with 4831 vertices, and the calculating time step was 0.001 s .

3.2 Governing equations

The variables in this model are the species in the solid phase, the species in the vapor phase, porosity, pressure inside the particle, velocity of the volatiles, and temperature, assuming that solids and volatiles are in thermal equilibrium. Table 4 shows the governing equations of the model, one equation for each model variable. Equation (1) is the conservation of the solid species accounting for the decomposition of wheat and the generation and decomposition of activated wheat. Equation (2) is the conservation of the vapor species, which includes the generation of volatiles and the mass convection of the vapor species, which is dominant over the volatiles diffusion, and for that reason, the mass diffusion term could be neglected.⁶ Equation (3) is the conservation of energy and includes the heat generation from the reactions, heat convection from the volatiles release, and heat conduction. Heat transfer due to the volatiles diffusion is considered not to be significant,²² so it is not included in the energy balance. The boundary condition of the energy balance can be found in Eq. (4), and it describes the surface heating of the particle by thermal convection and thermal radiation. Equation (5) describes how the porosity changes with a changing density of the solid particle. Eq. (6) describes how the pressure in the particle changes according to the ideal gas law, and Eq. (7) describes how the velocity of the volatiles changes according to Darcy’s law.

The finite element method has been used to discretize in space the partial differential equations (PDEs). The resulting ODEs are discretized in time using the Crank-Nicolson method, which is a finite difference method of discretization in time. The solution at the previous time is determined from a known initial solution or from a previous solution to the model, and the solution at the current time is determined from the previous solution. The final system of linear equations is solved using FEniCS open-source software.

Table 4: Governing equations.

Parameter	Equation
Mass balance (solid phase)	$\frac{\partial \rho_{s,i}}{\partial t} = \sum_r \nu_{r,i} \frac{\partial \xi_r}{\partial t}$ (1)
Mass balance (vapor phase)	$\frac{\partial}{\partial t} (\varepsilon \rho_{v,i}) + \nabla \cdot (\rho_{v,i} \mathbf{u}) = \sum_r \varepsilon \nu_{r,i} \frac{\partial \xi_r}{\partial t}$ (2)
Energy balance	$(\rho_s C_{p,s} + \varepsilon \rho_v C_{p,v}) \frac{\partial T}{\partial t} + \mathbf{u} \rho_v C_{p,v} \cdot \nabla T - \nabla \cdot (\lambda \nabla T)$ $= - \sum_r \Delta H_r \frac{\partial \xi_r}{\partial t}$ (3)
Boundary condition	$\hat{n} \cdot \lambda \nabla T = h(T - T_\infty) + \epsilon \sigma (T^4 - T_\infty^4)$ (4)
Porosity	$\varepsilon = 1 - (1 - \varepsilon_0) \frac{\rho_s}{\rho_{s,0}}$ (5)
Pressure	$P = \frac{\rho_v R T}{M W_v}$ (6)
Velocity	$\mathbf{u} = \frac{-\kappa}{\mu} \nabla P$ (7)

Table 5: Dimensionless equations.

Parameter	Equation
Mass balance (solid phase)	$\frac{\partial \bar{\rho}_{s,i}}{\partial \bar{t}} = \sum_r \nu_{r,i} \bar{A}_r e^{-\bar{E}_r / \bar{T}} \bar{\rho}_s$ (8)
Mass balance (vapor phase)	$\frac{\partial}{\partial \bar{t}} (\varepsilon \bar{\rho}_{v,i}) + \bar{\nabla} \cdot (\bar{\rho}_{v,i} \bar{\mathbf{u}}) = \sum_r \nu_{r,i} \bar{A}_r e^{-\bar{E}_r / \bar{T}} \bar{\rho}_s \left(\frac{\rho_{s,0} R T_0}{P_0} \right)$ (9)
Energy balance	$(\bar{\rho}_s \bar{C}_{p,s} + \varepsilon \bar{\rho}_v \frac{P_0}{\rho_{s,0} R T_0} \bar{C}_{p,v}) \frac{\partial \bar{T}}{\partial \bar{t}} + \bar{\mathbf{u}} \bar{\rho}_v \frac{P_0}{\rho_{s,0} R T_0} \bar{C}_{p,v} \cdot \bar{\nabla} \bar{T} - \bar{\nabla} \cdot (\bar{\lambda} \bar{\nabla} \bar{T})$ $= - \sum_r \frac{\Delta H_r}{T_0 C_{p,s,0}} \bar{A}_r e^{-\bar{E}_r / \bar{T}} \bar{\rho}_s$ (10)
Boundary condition	$-\hat{n} \cdot \bar{\lambda} \bar{\nabla} \bar{T} = \frac{h_0 d_p}{\lambda_0} (\bar{T} - \bar{T}_\infty) + \frac{\epsilon \sigma d_p T_0^3}{\lambda_0} (\bar{T}^4 - \bar{T}_\infty^4)$ (11)
Porosity	$\varepsilon = 1 - (1 - \varepsilon_0) \frac{\bar{\rho}_s}{\rho_{s,0}}$ (12)
Pressure	$\bar{P} = \bar{\rho}_v \bar{T}$ (13)
Velocity	$\bar{\mathbf{u}} = -\frac{\kappa_0 P_0}{\mu \alpha_0} \bar{\kappa} \bar{\nabla} \bar{P}$ (14)

4 Results and discussion

4.1 Dimensional analysis

The dimensionless form of the governing equations is given in Table 5, where the parameters with a bar above them refer to the dimensionless model parameters. Nondimensionalization has been carried out in order to facilitate the solver solution when comparing orders of magnitude, to determine the relative importance of the different terms in the governing equations, and to identify which processes are more significant in pyrolysis.

Table 6: Parameters and groups used to nondimensionalize the model equations.

Parameter	Value or expression
$\bar{\rho}_s$	$\frac{\rho_s}{\rho_{s,0}}$
$\bar{\rho}_v$	$\frac{\rho_v RT_0}{P_0 MW_v}$
\bar{T}	$\frac{T}{T_0}$
\bar{P}	$\frac{P}{P_0}$
$\bar{\mathbf{u}}$	$\frac{\tau}{d_{particle}} \mathbf{u}$
$\bar{\nabla}$	$d_{particle} \nabla$
$\bar{\lambda}$	$\varepsilon_0 \frac{\lambda_G}{\lambda_0} + \frac{\rho_B}{\rho_{B,0}} \frac{\lambda_B}{\lambda_0} + \left(1 - \frac{\rho_B}{\rho_{B,0}} \frac{\lambda_C}{\lambda_0} + \frac{13.5\sigma T^3 d_{pore}}{\varepsilon \lambda_0}\right)$
\bar{A}_r	τA_r
\bar{E}_r	$\frac{E_r}{RT_0}$
$\bar{\kappa}$	$\frac{\rho_B}{\rho_{B,0}} \frac{\kappa_B}{\kappa_0} + \left(1 - \frac{\rho_B}{\rho_{B,0}}\right) \frac{\kappa_C}{\kappa_0}$

The definition of the dimensionless parameters that appear in the dimensionless equations can be found in Table 6, and the values of the dimensionless groups that appear in the dimensionless equations are given in Table 7 for the different reactor temperatures. Each dimensionless group is individually linked to the dimensionless equation in which it appears. The dominant heat transfer mechanisms can be identified by comparing the dimensionless groups in front of the terms in the energy balance. Using the values for the reactor temperature of 700°C as example, it can be observed that the coefficients of heat convection, thermal radiation, and heat generation from the reactions are 0.42, 0.12, and 0.068, respectively, meaning that the heat transfer from the reactor environment to the particle is the dominant heating mechanism over the particle self-heating from the heat of reaction. Among the external heating mechanisms, it also shows that heat convection is dominant over thermal radiation. The term of the heat of reaction contains an exponential, which means that at higher temperatures that term might become more influential. The coefficient that appears in front of the volatile terms is very small, 0.045, and it barely changes for the different reactor temperatures. From this observation, it can be assumed that the volatile terms do not have a significant impact on the temperature of the particle, therefore, the

influence of the volatiles convection in the energy balance could be neglected, and the heat capacity of the volatiles is not as influential as the heat capacity of the solids. The mass transfer by convection of the vapor phase is still relevant in the mass balance, given that the velocity of the vapor has a dimensionless coefficient of 4794, and the generation of volatiles has a coefficient of 22. However, the generation term has an exponential that depends on the temperature, so its influence can significantly vary at higher temperatures.

Some earlier work attributed a cooling effect on the particle to the release of volatiles from the particle by convection.^{22,26,27} For the studied pyrolysis conditions in this work, it has been found that the relative importance of the aforementioned cooling effect caused by the volatiles convection is not significant in comparison to the other heat transfer mechanisms. Anca-Cuoco et al.⁶ also reported a low influence of the volatiles convection on the temperature distribution of the particle. However, the volatiles convection term in the energy balance should not be neglected if the volatiles inside the particle undergo secondary reactions before they have time to leave the particle. If the volatiles remain in the particle long enough to undergo secondary pyrolysis, the enthalpy of the secondary reactions might influence the temperature of the particle.

Table 7: Values of the dimensionless groups appearing in the dimensionless form of the governing equations.

Group	200°C	300°C	400°C	500°C	600°C	700°C	Eq.
$\tau = \frac{d_{particle}^2}{\alpha_0}$	685.1	686.8	689.9	692.8	695.5	695.5	
$\frac{\rho_{s,0}RT_0}{P_0}$	19.7	20	20.7	21.3	22	22	(9)
$\frac{P_0}{\rho_{s,v}RT_0}$	0.05	0.049	0.048	0.047	0.045	0.045	(10)
$\frac{\Delta H_r}{T_0 C_{p,s,0}}$	0.078	0.076	0.073	0.07	0.068	0.068	(10)
$\frac{\epsilon \sigma d_{particle} T_0^3}{\lambda_0}$	0.09	0.094	0.1	0.113	0.123	0.123	(11)
$\frac{h_0 d_{particle}}{\lambda_0} = \text{Bi}$	0.55	0.5	0.48	0.46	0.43	0.42	(11)
$\frac{\kappa_0 P_0}{\mu \alpha_0}$	4723	4734	4756	4776	4794	4794	(14)

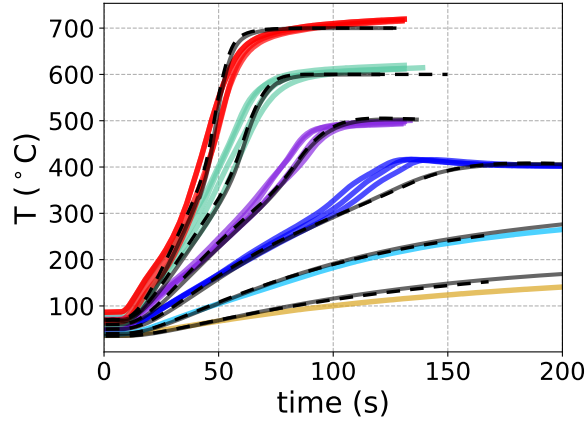


Figure 4: Measured center temperature of a pellet at different reactor temperatures: 200°C (yellow), 300°C (cyan), 400°C (dark blue), 500°C (purple), 600°C (green) and 700°C (red); and calculated center temperature using a 1D spherical model with $\lambda_B = 0.15 \text{ W m}^{-1} \text{ K}^{-1}$ (black dashed line) and a 3D cylindrical model with $\lambda_B = 0.11 \text{ W m}^{-1} \text{ K}^{-1}$ (grey solid line).

4.2 Comparison of 1D and 3D modeling results

4.2.1 Center temperature of the particle

The calculated center temperature using both 1D and 3D models is validated against the experimental center temperature for each reactor temperature in Figure 4. The multiple colored lines corresponding to each reactor temperature represent different repetitions of the same experiment, and the black lines are the different calculated solutions for the spherical one-dimensional SPM and the cylindrical three-dimensional SPM. It should be noticed that the variability of the measured data is probably due to the use of a different pellet for each experiment, which entails a natural variability in the pellet and some variations in the thermocouple manual insertion.

The curves at 200°C and 300°C in Figure 4 render the particle heating only, since the temperatures reached before 200s are still too low for pyrolysis, therefore they are useful to fit the thermophysical properties of the biomass during the heating period.

The experimental center temperatures of the pellets at the reactor temperatures of 400°C, 600°C and 700°C seem to reach a maximum temperature slightly higher than the correspond-

ing reactor temperature.

The experimental center temperature at the reactor temperature of 400°C displays a small peak or shoulder just before it stabilizes to the corresponding reactor temperature. When this happens, it means that the rate of heat generation is higher than the rate of heat transfer from the particle to the environment. This behavior is believed to be caused by exothermic reactions happening just before all the devolatilization reactions finish, that is why it is associated with the decomposition of a solid intermediate into a solid product.⁸ The exothermic reaction causing the peak might be related to char formation, which is favoured at low heating rates.²⁸ After the peak, the particle's temperature reaches equilibrium with the reactor temperature due to thermal convection.²⁹

The pellets at the reactor temperatures of 600°C and 700°C seem to experience a slight overheating caused by secondary reactions that are enabled at high pyrolysis temperatures. The secondary reactions are probably related to the dense volatiles released transforming further into light volatiles, and they are reported to be very exothermic.^{30,31}

The main thermophysical properties in the model are the biomass thermal conductivity and the biomass heat capacity. Their values in the model have a similar but opposite effect on the particle's heating. A larger heat capacity translates into a lower inner heating rate, and a larger thermal conductivity translates into a higher inner heating rate.

As previously mentioned in the model description in Section 3, two values of thermal conductivity have been compared for both the one-dimensional and the three-dimensional models. The accuracy of the models with each of the two values of thermal conductivity has been assessed with respect to the average of the experimental center temperature of the particle by means of the root mean squared error (RMS). The root mean square error calculates the difference between the calculated center temperature from each model and the mean of the measured center temperatures, and it is defined as $RMS = \frac{\sum_i^n (y1_i - y2_i)^2}{n}$, where $y1$ and $y2$ are the values to compare from two different curves, i denotes the value at a given time and n is the total number of values. The accuracy comparison can be found in Table 8.

Table 8: Error as root mean square (RMS) for the different reactor temperatures (T_∞) between the experimental data and the calculated center temperature using 1D and 3D models and different values of thermal conductivity of biomass λ_B .

T_∞ (°C)	RMS (1D)	RMS (3D)	λ_B (W m ⁻¹ K ⁻¹)
200	12	18.1	0.11
	12.8	23.6	0.15
300	6.8	7.5	0.11
	5.5	17.9	0.15
400	34.8	20.7	0.11
	22.2	15.6	0.15
500	39.4	14.3	0.11
	12.8	18.1	0.15
600	54.2	26.8	0.11
	25.3	19.3	0.15
700	61.1	23.3	0.11
	27.1	37.2	0.15
Mean RMS	34.7	18.5	0.11
	17.6	22	0.15

It can be observed that the mean RMS for the 3D model is lower when $\lambda_B = 0.11$, and that the mean RMS for the 1D model is lower when $\lambda_B = 0.15$, in consequence, these are the respective thermal conductivity values used in each SPM model. It makes sense that the 1D model fits the experimental data better with a higher thermal conductivity, given that a spherical shape has a lower ratio of surface over volume and it takes longer to heat than a finite cylindrical shape, which can only be rendered with the 3D model. The mean RMS for the 1D model ranges from 17.6 to 34.7 (17.1 units of difference), and the mean RMS for the 3D model ranges from 18.5 to 22 (3.5 units of difference). From the previous observation, it can be concluded that the impact of the thermal conductivity value in the SPM is much more significant for the 1D model than for the 3D model, and therefore a 3D model would be compatible with a wider range of biomass types and it would allow for a higher degree of uncertainty when the values or correlations that describe the biomass characteristics are not known in detail.

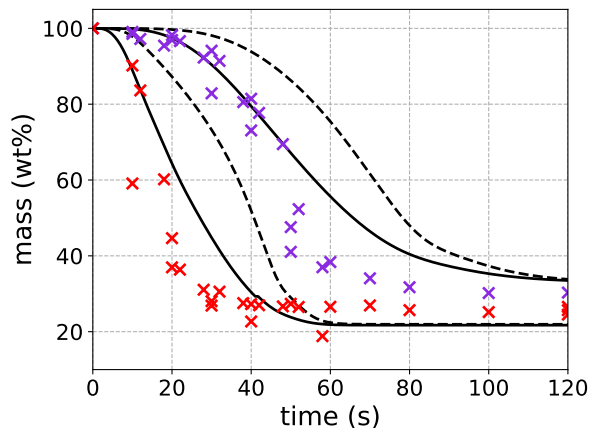


Figure 5: Calculated (3D: solid line and 1D: dash line) and measured (crosses) mass loss of a straw pellet at 500°C (purple) and 700°C (red). Including ash, which is 7.4% of the dry initial mass.

4.2.2 Mass loss

The experimental and calculated mass loss of a pellet at three reactor temperatures are shown in Figure 5. The colored symbols are the experimental data and the black lines are the calculated data for the 1D and 3D models.

For all of the reactor temperatures, the predicted decomposition should be steeper at an earlier time. A possible source of error in this case could be the values of the kinetic parameters used in the kinetic mechanism, given that they were originally determined for the pyrolysis of a wheat straw pellet, but for operating conditions in the range of 126.85 and 374.85°C, which is lower than the reactor temperatures used in this study. However, the calculated mass loss using the 3D model is closer to the experimental results than the mass loss calculated using the 1D model, which means that despite the center temperature predicted is same for both models (see Figure 4), the way in which the heat is transferred and distributed inside the particle is different and it influences the rate of mass loss. The predicted char yield, as it can be observed still in Figure 5, is the same for both models, and it is close to the experimental char yield.

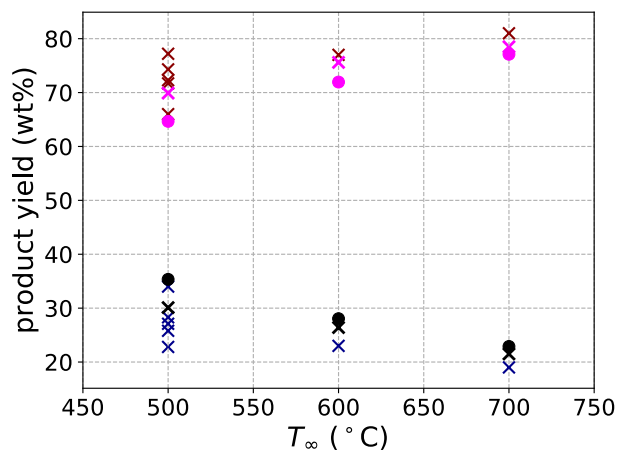


Figure 6: Char and volatile yields for the different reactor temperatures after pyrolysis has finalized. Experimental and literature^{32–36} (crosses), calculated (circles), volatile (pink, red) and char (black, blue).

4.2.3 Product yields

The experimental char yields obtained in this study, in addition to the experimental char yields obtained from the literature, and the calculated char yields using the SPM for the reactor temperatures of 500°C, 600°C and 700°C can be found in Figure 6. The calculated char yields are obtained with respect to the original biomass weight once pyrolysis has finalized, and they include ash. The volatile yields are calculated by difference. The char amount decreases with an increasing reactor temperature, and the opposite is true for the volatile yield.

The product yields obtained experimentally and calculated in this work, are similar to the reported experimental values found in the literature. For the reactor temperature of 500°C there has been more literature values found, and it can be observed the char yield is in the range of 20–40% and the volatile yield is in the range of 60–80%, this variability of values reflects the impact of the different biomass types and operating conditions on the final product yields.

Table 9: Computational time comparison between a one-dimensional and a three-dimensional model of a sphere of diameter 9 mm undergoing pyrolysis and without taking into account the gas phase.

T_∞ (°C)	Model	Dimensionless time	Computational time
200	1D/3D	0.1/0.1	11 s/98 min
300	1D/3D	0.1/0.1	11.1 s/133 min
400	1D/3D	0.1/0.1	11.3 s/241 min
500	1D/3D	0.1/0.1	12 s/496 min
600	1D/3D	0.1/0.08	12.6 s/1 week
700	1D/3D	0.1/0.06	13.1 s/1 week

4.2.4 Computational costs

A time comparison between solving the one-dimensional SPM, excluding the process of mass convection, and the three-dimensional SPM of the same particle shape and size as the one-dimensional model has been carried out. Table 9 shows a comparison of the time required to run a one-dimensional versus a three-dimensional model of a sphere of the same radius. The computer specifications are Intel[®] Xeon[®] Processor E5-1620 v2 and 15GB of RAM. The dimensionless time for the three-dimensional model and reactor temperatures of 600 and 700°C is shorter than the time used in the other instances because at that time the process has already finished, and without any other mechanisms implemented in the model following the volatile release from the particle, the calculations in three-dimensions for those reactor temperatures just slow down and stop. Despite that, it can be observed that the computational time increase using the three-dimensional model is significant.

Given the significant increase in computational time that the three-dimensional single particle model entails and its small gain in accuracy prediction of the center temperature versus the one-dimensional model, in this case a three-dimensional model does not seem a justifiable model choice. However, the three-dimensional model enables additional featured results, as detailed in the following section.

4.3 Additional featured results from 3D modelling

4.3.1 Inner temperature distribution of the particle

The experimental and calculated temperature at the center and at the position of 2 mm from one end of the cylindrical particle are shown in Figure 7 for three reactor temperatures. Additionally, the calculated surface temperature at one end of the cylindrical particle is also shown in the same figure. It can be observed how the temperature curves from the center and at 2 mm start heating with a bit of delay with respect to the surface temperature. For all the three reactor temperatures, a steep rise of the measured temperature at the 2 mm position could be observed during the first 10 s after the particle starts heating, this steep rise was not seen in the model. This behavior observed in the experimental data is probably caused by an increase in heating by convection and thermal radiation due to a damaged pellet surface in the area where the thermocouple was inserted, however an increase in thermal conduction through the thermocouple wire could also have contributed.

For the sake of visual comparison of the heating of the particle, Figure 8 shows the internal temperature distribution of the cylindrical pellet for three reactor temperatures and at four given times, the given times are 15 s, 30 s, 50 s and 100 s from when the particle started heating. The temperature range in the legend is the same for all the reactor temperatures to allow a visual comparison across conditions. The pellets start heating from the surface and the heat is then transferred towards the center. The pellets at the reactor temperatures of 500°C, 600°C and 700°C already reached their respective reactor temperatures after 100 s.

4.3.2 Heating rate inside the particle

Each pellet at each reactor temperature heats with a different inner heating rate, which is not constant and might change with time depending on the enthalpy of reaction and on how the thermophysical properties of the biomass change with temperature. Figure 9 shows the derivative of the inner temperature curves shown in Figure 7. The surface reaches its

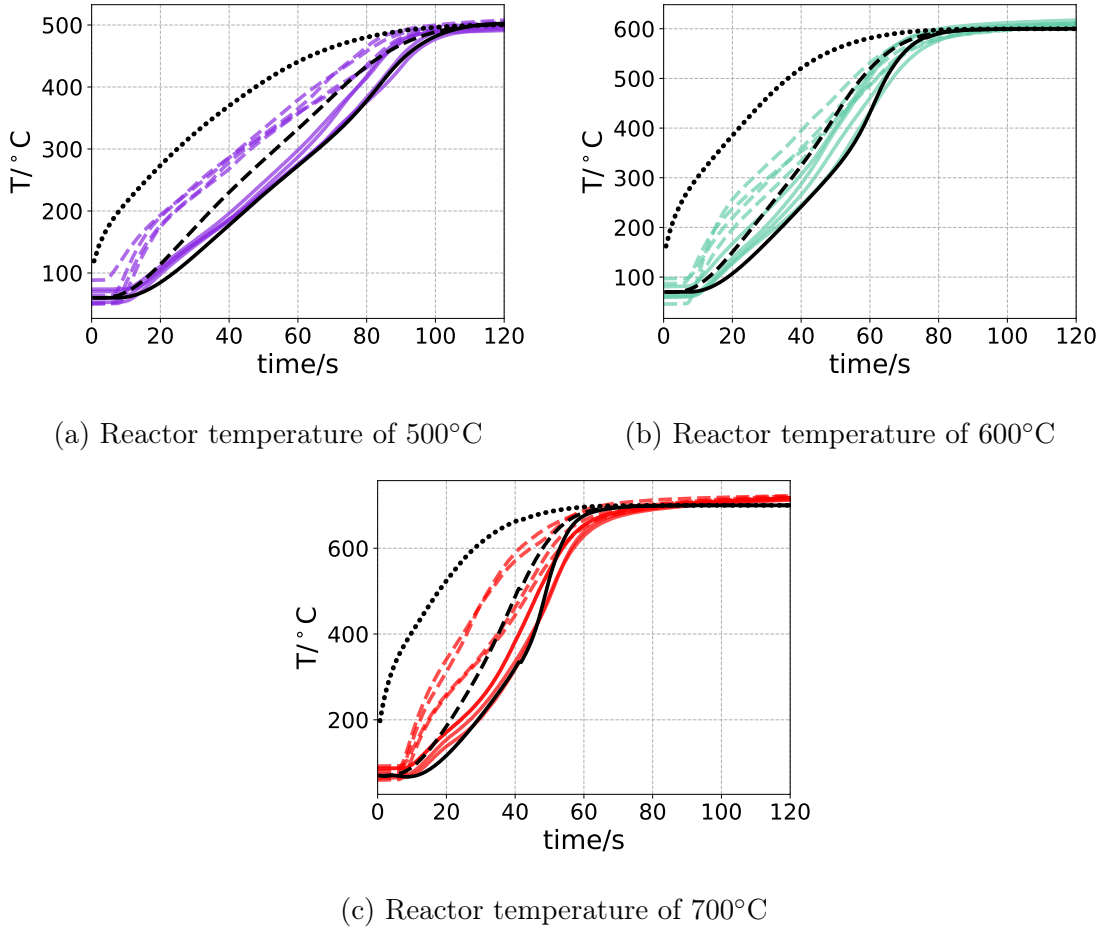


Figure 7: Calculated (black) and measured (colored) inner temperature of a pellet. Center temperature (solid line), temperature at 2 mm from the surface (dashed line), and predicted surface temperature (dotted line).

maximum heating rate from the first moment and then decreases as the difference between the surface temperature and the reactor temperature decreases. It can be noticed that for all the reactor temperatures, but more evidently for the reactor temperature of 700°C, the heating rate at the center of the particle reaches a value higher than the heating rate reached at 2 mm from the surface. The increased heating rate at the center of the particle is always observed towards the end of the heating period. This behavior makes sense with what was already experimentally observed in Figure 4 and discussed for the reactor temperature of 400°C, in which an increase in heat generation from the pyrolysis reactions seems to take place just before devolatilization ends.

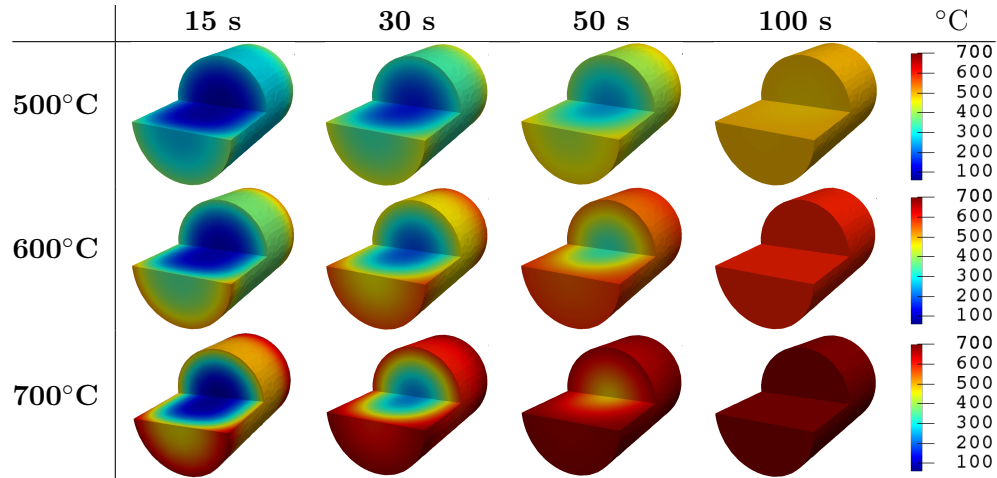
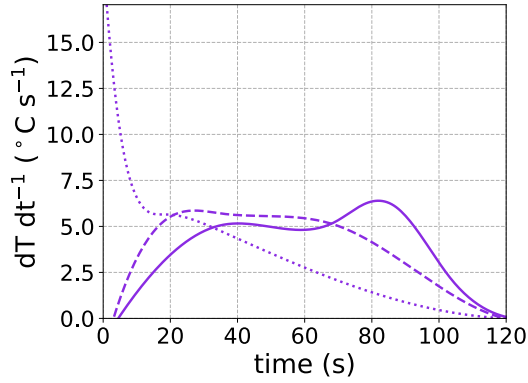


Figure 8: Calculated temperature distribution of the pellet for different reactor temperatures at the selected times.

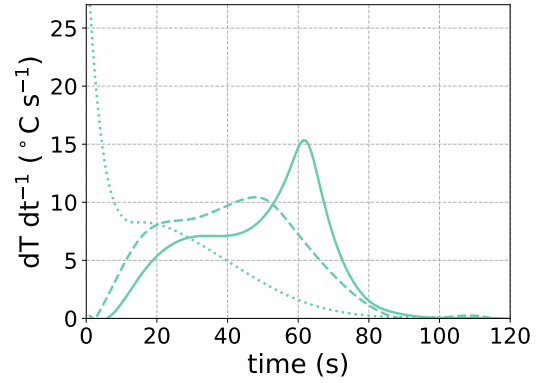
The heating rate of the particle has not been found in previous literature by the authors, but in the work of Lu et al.³⁷ they show the center temperature of a particle of 9.5 mm of diameter undergoing pyrolysis, and in their case, the temperature curve clearly displays an increase in heating rate towards the end of pyrolysis.

4.3.3 Porosity distribution

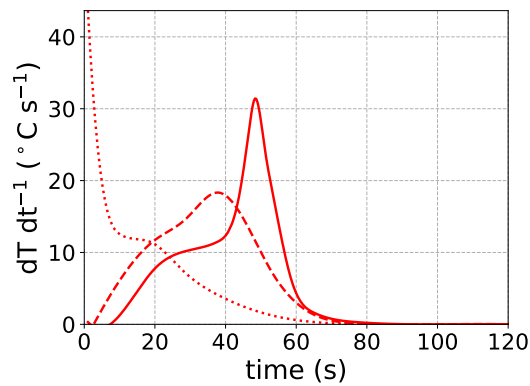
The radial distribution of the porosity in the particle for the 3D model can be found in Figure 10. The reactor temperature of 600°C and four given times (15, 30, 50 and 100 s) have been used as example. The 3D cylindrical particle has a different radial porosity distribution along the longitudinal axis. The porosity increases more quickly at a position nearer to the particle's longitudinal end than at the center. The inner porosity patterns are related to the inner heating patterns, and the heating patterns are related to the shape and the size of the particle. If the targeted pyrolysis product is the pyrolyzed biomass and a desired porosity fraction or profile is to be obtained, controlling the pyrolysis time, as can be observed from this figure, is crucial. The highest difference in porosity between the the two positions in the particle can be observed for the curves at 50 s, time at which the respective heating rate curves overlap in Fig. 9. At 50 s the heating rate at 2 mm position has already



(a) Reactor temperature of 500°C.



(b) Reactor temperature of 600°C



(c) Reactor temperature of 700°C

Figure 9: Inner heating rate at the center (solid line), at 2 mm from the surface (dashed line), and at the surface (dotted line) of a cylindrical particle undergoing pyrolysis.

reached its maximum and that is reflected by the increased porosity profile, and the heating rate at the center has yet to increase to its maximum value. The curves at 100 s show the final porosity profile of the particle, it is practically the same for both inner positions and also in both cases they seem to reach a higher value of porosity at the radial center and at the radial surface than in between. This can be caused by an increased heating rate at the radial center and radial surface of the particle, following a similar pattern as in Fig. 9 where the heating rate at the longitudinal center and longitudinal surface of the cylindrical particle also reach a higher value than in in between.

The porosity at the center of the 3D particle for two reactor temperatures can be found Figure 11. It can be observed that the porosity of the particle at the highest reactor temper-

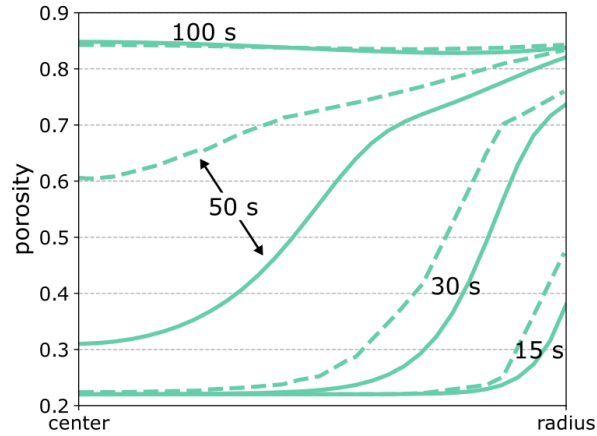


Figure 10: Porosity evolution with time along the radial axis and at the center of the particle (solid line) and at 2 mm from the longitudinal end of particle (dashed line) of a cylindrical particle undergoing pyrolysis at the reactor temperature of 600°C.

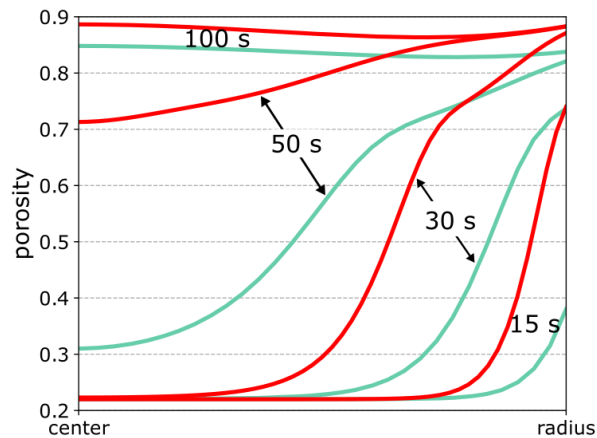


Figure 11: Porosity evolution with time at the center of a cylindrical particle undergoing pyrolysis at the reactor temperature of 600°C (green) and 700°C (red).

ature increases more quickly, and it also reaches a higher final porosity. This figure is just to exemplify the effect that the operating temperature has on the final porosity distribution. It should be noted that the porosity curves at the center of the particle are the same for the 1D spherical particle as in the 3D cylindrical particle, given that the center temperature showed in Figure 4 is the same for both models, with the difference of the length of the radius.

Figure 12 shows the porosity distribution of the pellet for the different reactor temperatures and at different given times. The porosity has been calculated with a correlation

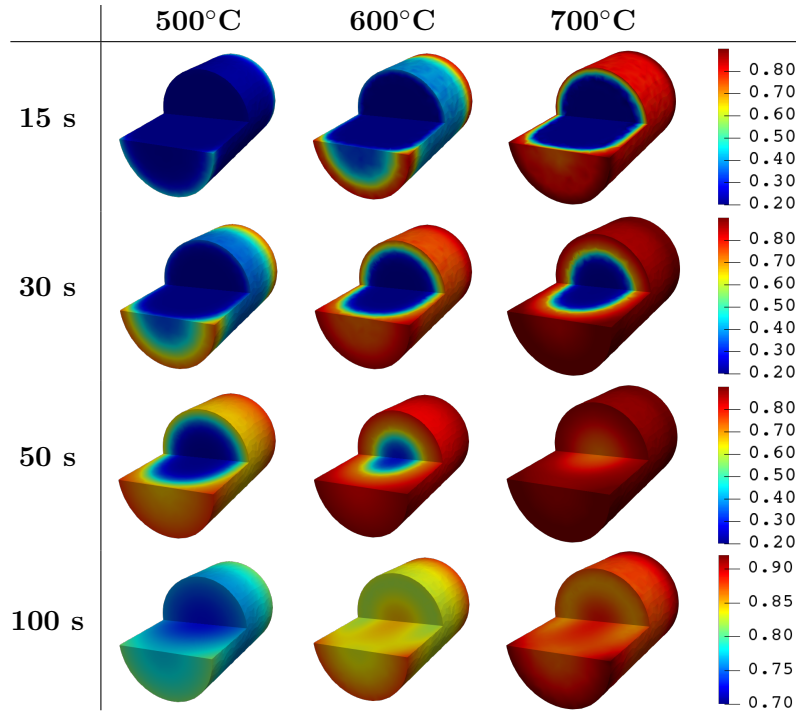


Figure 12: Calculated porosity distribution of the pellet for different reactor temperatures at the selected times; the legend is porosity.

(Table 3) that depends on the decomposition of the solids in the particle. The time to reach the final porosity value for each reactor temperature is 63 s (700°C), 85 s (600°C), 130 s (500°C), 180 s (400°C), 300 s (300°C), and for the lowest reactor temperature is 2000 s (200°C).

When the aim of biomass pyrolysis is to produce activated carbon, a feature of interest would be the char microporosity volume.³⁸ In the current model the pore size is not included, given that the porosity is described as a fraction. Modelling the single particle with a mesh that renders the microporosity would be useful to study the changes in pores size, but it would not be feasible due to its high computational cost. The porosity observed at the center of the pellet and at 100 s for the particles at the reactor temperatures of 600°C and 700°C is larger than the porosity observed between the center and the surface of the particle. This increased porosity at the center is a result of the behavior observed for the heating rate in Figure 9, in which the center reaches a higher heating rate than the position at 2 mm from

the surface.

5 Conclusions

One-dimensional and three-dimensional single particle models were developed to describe the pyrolysis of wheat straw, both have been successfully validated against experimental data. A comprehensive assessment of the impact of dimensionality of the SPMs have been conducted and compared their performances in order to gain a systematic understanding of the accuracy of predicted results, predictive capability and computational costs, etc.

The results shown that the shape of the particle and the model dimensionality influence the inner heating profile and the rate of mass loss, and that the assumption of a one-dimensional model decreases the model accuracy with respect to the heating profile of the particle. These results suggest that three-dimensional models are needed to fully understand pyrolysis of large biomass particles, while the one-dimensional single particle model is more sensitive to the values given for the model thermophysical parameters, making the three-dimensional single particle model compatible with a wider range of biomass types.

The computational costs have been quantitatively compared and concluded that the three-dimensional single particle model requires a significant longer computational time, while its small gain in accuracy prediction of the center temperature versus the one-dimensional model seem not a justifiable model choice, however, it offers additional featured results, including insightful inner temperature distribution, heating rate inside the particle and porosity distribution. To improve the prediction of the pyrolysis behavior of a biomass particle in the thermally thick regime, the model parameters that describe the characteristics of the particle and the heating mechanisms could be further optimised.

Future work will involve the assessment of one-dimensional and three-dimensional SPMs with implementation of the detailed secondary reactions taking place inside the particle for the gas phase that allow for the circulation of volatiles and nitrogen in both directions, in

and out of the particle, and detailed experimental data on the pyrolysis products.

Nomenclature

Symbols

ϵ	emissivity
κ	permeability, m^2
μ	dynamic viscosity, Pa s
$\nu_{r,i}$	stoichiometry of the species i in the reaction r
ρ	density, kg m^{-3}
σ	Stefan-Boltzmann constant, $\text{W m}^{-2} \text{K}^{-4}$
τ	dimensionless time
ε	porosity
ξ_r	extent of reaction, kg

Letters

A	pre-exponential factor, s^{-1}
CL	characteristic length, m
C_p	heat capacity, $\text{J kg}^{-1} \text{K}^{-1}$
E	activation energy, J mol^{-1}
P	pressure, Pa
P_0	atmospheric pressure
R	gas constant, $\text{J mol}^{-1} \text{K}^{-1}$
T	temperature, K
T_∞	reactor temperature, K
ΔH_r	heat of reaction, J kg^{-1}
λ	thermal conductivity, $\text{W m}^{-1} \text{K}^{-1}$
\mathbf{u}	velocity, m s^{-1}

\mathbf{v}_{N_2}	carrier gas velocity, m s^{-1}
d_{pore}	pore diameter, m
d_p	particle diameter, m
h	heat transfer coefficient, $\text{W m}^{-2} \text{K}^{-1}$
k	rate constant, s^{-1}
MW	molecular weight, kg mol^{-1}
SPM	Single Particle Model
r	reaction

Subscripts

∞	surrounding condition
0	initial condition
B	biomass (wheat + activated wheat)
C	char
G	gas
T	tar
i	species in the solids or volatiles
r	reaction
s	solids (biomass + char)
v,V	vapor, volatiles (gas + tar)

Acknowledgement

The authors acknowledge the financial support provided by Scottish Funding Council - Global Challenge Research Fund (SFC1204-114), the Energy Technology Partnership - Postgraduate and Early Career Researchers Exchanges (PECRE) Grant and the Academy of Finland financed project with no. 321598 - Chemical challenges in gasification of biomass and waste, and the technical support from Luis Bezerra.

References

- (1) Bennadji, H.; Smith, K.; Shabangu, S.; Fisher, E. Low-Temperature Pyrolysis of Woody Biomass in the Thermally Thick Regime. *Energy Fuels* **2013**, *27*, 1453–1459.
- (2) Di Blasi, C. Modeling chemical and physical processes of wood and biomass pyrolysis. *Prog. Energy Combust. Sci.* **2008**, *34*, 47–90.
- (3) Pyle, D.; Zaror, C. Heat transfer and kinetics in the low temperature pyrolysis of solids. *Chem. Eng. Sci.* **1984**, *39*, 147 – 158.
- (4) Corbetta, M.; Frassoldati, A.; Bennadji, H.; Smith, K.; Serapiglia, M. J.; Gauthier, G.; Melkior, T.; Ranzi, E.; Fisher, E. M. Pyrolysis of Centimeter-Scale Woody Biomass Particles: Kinetic Modeling and Experimental Validation. *Energy Fuels* **2014**, *28*, 3884–3898.
- (5) Ranzi, E.; Cuoci, A.; Faravelli, T.; Frassoldati, A.; Migliavacca, G.; Pierucci, S.; Sommariva, S. Chemical Kinetics of Biomass Pyrolysis. *Energy Fuels* **2008**, *22*, 4292–4300.
- (6) Anca-Couce, A.; Zobel, N. Numerical analysis of a biomass pyrolysis particle model: Solution method optimized for the coupling to reactor models. *Fuel* **2012**, *97*, 80 – 88.
- (7) Babu, B. V.; Chaurasia, A. S. Heat transfer and kinetics in the pyrolysis of shrinking biomass particle. *Chem. Eng. Sci.* **2004**, *59*, 1999 – 2012.
- (8) Park, W. C.; Atreya, A.; Baum, H. Experimental and theoretical investigation of heat and mass transfer processes during wood pyrolysis. *Combust. Flame* **2010**, *157*, 481–494.
- (9) Ghabi, C.; Benticha, H.; Sassi, M. Two-Dimensional Computational Modeling and Simulation of Wood Particles Pyrolysis in a Fixed Bed Reactor. *Combustion Science and Technology* **2008**, *180*, 833–853.

- (10) Wickramarachchi, W.; Narayana, M. Pyrolysis of single biomass particle using three-dimensional Computational Fluid Dynamics modelling. *Renewable Energy* **2020**, *146*, 1153 – 1165.
- (11) Blasi, C. D. Physico-chemical processes occurring inside a degrading two-dimensional anisotropic porous medium. *Int. J. Heat Mass Transfer* **1998**, *41*, 4139 – 4150.
- (12) Nolan Ciesielski, P.; Crowley, M.; Nimlos, M.; Sanders, A.; M. Wiggins, G.; J Robichaud, D.; Donohoe, B.; Foust, T. Biomass Particle Models with Realistic Morphology and Resolved Microstructure for Simulations of Intra-Particle Transport Phenomena. *Energy Fuels* **2014**, *29*.
- (13) Wickramarachchi, W.; Narayana, M. Pyrolysis of single biomass particle using three-dimensional Computational Fluid Dynamics modelling. *Renewable Energy* **2020**, *146*, 1153–1165.
- (14) Gentile, G.; Debiagi, P. E. A.; Cuoci, A.; Frassoldati, A.; Ranzi, E.; Faravelli, T. A computational framework for the pyrolysis of anisotropic biomass particles. *Chemical Engineering Journal* **2017**, *321*, 458–473.
- (15) Karlström, O.; Brink, A.; Hupa, M. Biomass Char Nitrogen Oxidation - Single Particle Model. *Energy Fuels* **2013**, *27*, 1410–1418.
- (16) Karlström, O.; Brink, A.; Hupa, M. Desorption kinetics of CO in char oxidation and gasification in O₂, CO₂ and H₂O. *Combust. Flame* **2014**, *162*.
- (17) Lanzetta, M.; Blasi, C. D. Pyrolysis kinetics of wheat and corn straw. *J. Anal. Appl. Pyrolysis* **1998**, *44*, 181 – 192.
- (18) Churchill, S.; Bernstein, M. A correlating equation for forced convection from gases and liquids to a circular cylinder in crossflow. *J. Heat Transfer* **1977**, *99*, 300–306.

- (19) Blondeau, J.; Jeanmart, H. Biomass pyrolysis at high temperatures: Prediction of gaseous species yields from an anisotropic particle. *Biomass Bioenergy* **2012**, *41*, 107–121.
- (20) Grønli, M. G.; Melaaen, M. C. Mathematical Model for Wood Pyrolysis Comparison of Experimental Measurements with Model Predictions. *Energy Fuels* **2000**, *14*, 791–800.
- (21) Lu, H.; Ip, E.; Scott, J.; Foster, P.; Vickers, M.; Baxter, L. L. Effects of particle shape and size on devolatilization of biomass particle. *Fuel* **2010**, *89*, 1156 – 1168.
- (22) Blasi, C. D. Modelling the fast pyrolysis of cellulosic particles in fluid-bed reactors. *Chem. Eng. Sci.* **2000**, *55*, 5999 – 6013.
- (23) Lam, P. S. W.; Sokhansanj, S.; Bi, X.; Lim, J.; Naimi, L.; Hoque, M.; Mani, S.; Ray Womac, A.; Philip Ye, X.; Narayan, S. Bulk Density of Wet and Dry Wheat Straw and Switchgrass Particles. *Applied engineering in agriculture* **2008**, *24*, 351–358.
- (24) Lu, D.; Tabil, L.; Wang, D.; Wang, G. Manufacturing Wheat Straw Pellet with Wood Waste and Binders. *CSBE/SCGAB annual conference* **2013**,
- (25) Mason, P.; Darvell, L.; Jones, J.; Williams, A. Comparative Study of the Thermal Conductivity of Solid Biomass Fuels. *Energy Fuels* **2016**, *30*, 2158–2163.
- (26) Janse, A.; Westerhout, R.; Prins, W. Modelling of flash pyrolysis of a single wood particle. *Chemical Engineering and Processing: Process Intensification* **2000**, *39*, 239 – 252.
- (27) Bilbao, R.; Millera, A.; Murillo, M. B. Temperature profiles and weight loss in the thermal decomposition of large spherical wood particles. *Ind. Eng. Chem. Res.* **1993**, *32*, 1811–1817.
- (28) Watanabe, H.; Morinaga, Y.; Okada, T.; Okazaki, K. Experimental and Numerical

- Investigation of Biomass Pyrolysis Process Focusing on Intra-Particle Heat Transfer. *14th International Heat Transfer Conference* **2010**, *3*, 161–168.
- (29) Haseli, Y.; van Oijen, J.; de Goey, L. Modeling biomass particle pyrolysis with temperature-dependent heat of reactions. *J. Anal. Appl. Pyrolysis* **2011**, *90*, 140 – 154.
- (30) Gómez, C.; Barontini, F.; Cozzani, V.; Velo, E. Influence of Secondary Reactions on the Heat of Pyrolysis of Biomass. *Ind. Eng. Chem. Res.* **2009**, *48*, 10222–10233.
- (31) Chen, Q.; Yang, R.; Zhao, B.; Li, Y.; Wang, S.; Wu, H.; Zhuo, Y.; Chen, C. Investigation of heat of biomass pyrolysis and secondary reactions by simultaneous thermogravimetry and differential scanning calorimetry. *Fuel* **2014**, *134*, 467 – 476.
- (32) Fu, P.; Bai, X.; Yi, W.; Li, Z.; Li, Y. Fast pyrolysis of wheat straw in a dual concentric rotary cylinder reactor with ceramic balls as recirculated heat carrier. *Energy Convers. Manage.* **2018**, *171*, 855 – 862.
- (33) Ates, F.; Tophanecioglu, S.; Putun, A. E. The Evaluation of Mesoporous Materials as Catalyst in Fast Pyrolysis of Wheat Straw. *International Journal of Green Energy* **2015**, *12*, 57–64.
- (34) Farooq, M. Z.; Zeeshan, M.; Iqbal, S.; Ahmed, N.; Asfand Yar Shah, S. Influence of waste tire addition on wheat straw pyrolysis yield and oil quality. *Energy* **2017**, *144*, 200 – 206.
- (35) Aqsha, A.; Tijani, M.; Moghtaderi, B.; Mahinpey, N. Catalytic Pyrolysis of Straw Biomasses (Wheat, Flax, Oat and Barley) and the Comparison of their Product Yields. *J. Anal. Appl. Pyrolysis* **2017**, *125*, 201–208.
- (36) Cheng, S.; Wei, L.; Zhao, X.; Huang, Y.; Raynie, D.; Qiu, C.; Kiratu, J.; Yu, Y.

Directly catalytic upgrading bio-oil vapor produced by prairie cordgrass pyrolysis over Ni/HZSM-5 using a two stage reactor. *AIMS Energy* **2015**, *3*, 227–240.

- (37) Lu, H.; Robert, W.; Peirce, G.; Ripa, B.; Baxter, L. Comprehensive Study of Biomass Particle Combustion. *Energy Fuels* **2008**, *22*.
- (38) Vyas, A.; Chellappa, T.; Goldfarb, J. L. Porosity development and reactivity changes of coal–biomass blends during co-pyrolysis at various temperatures. *J. Anal. Appl. Pyrolysis* **2017**, *124*, 79 – 88.